Computational and Theoretical Aspects of a Grain-Boundary Model at Finite Deformations

A.T. McBride, D. Gottschalk, B.D. Reddy, P. Wriggers and A. Javili

A model to describe the role of grain boundaries in the overall response of a polycrystalline material at small length scales subject to finite deformations is presented. Three alternative thermodynamically consistent plastic flow relations on the grain boundary are derived and compared using a series of numerical experiments. The numerical model is obtained by approximating the governing relations using the finite element method. In addition, the infinitesimal and finite deformation theories are compared, and the limitations of the former made clear.

1 Introduction

Modelling crystalline materials at small length scales requires a continuum theory that accounts for both the role of the grain boundary and for size-dependent effects. Numerous extended (gradient and non-local) continuum theories of single-crystal plasticity have been presented in the last two decades to capture size-dependent effects. These include the thermodynamically consistent gradient theory of Gurtin and co-workers and related works (see e.g. Gurtin, 2002; Gurtin and Needleman, 2005; Gurtin, 2006, 2008a).

Gurtin (2008b) presented a gradient crystal plasticity formulation that accounted for the role of the grain boundary. Critically, the grain-boundary model incorporates both the *misorientation in the crystal lattice* between adjacent grains, and the *orientation of the grain boundary* relative to the crystal lattice of the adjacent grains. The Gurtin (2008b) model is restricted to infinitesimal deformations. Recently, van Beers et al. (2013) have proposed and numerically implemented a theory similar to that of Gurtin (2008b) for incorporating grain boundaries into the gradient crystal plasticity theory of Evers et al. (2004). Our own contribution (Gottschalk et al., 2015) provides a theoretical and numerical investigation of the Gurtin (2008b) theory. The two measures of the defect structure at the grain boundary proposed by Gurtin were compared and a third measure introduced.

The objective of the current work is to extend the Gurtin (2008b) gradient crystal plasticity, grain-boundary theory to the finite-deformation regime. The basis for the extension is the finite-deformation crystal plasticity theory of Gurtin (2008a). In the spirit of Gurtin (2008b) for the infinitesimal-deformation theory, spatial intra-grain interaction and inter-grain interaction moduli are used to characterise the structure of the grain boundary. The proposed measure of the defect structure at the grain boundary involves the jump in the plastic distortion and a spatial measure of the grain boundary orientation. Two alternative measures of defect structure are also investigated. The systems of equations governing the response of the grain boundary are derived using a virtual power approach. The plastic flow relations on the grain boundary then follow from the reduced dissipation inequality. Three different flow relations, corresponding to the different grain boundary defect structures, are presented.

The structure of the presentation is as follows. The kinematics of the response in the grain and on the grain boundary are presented in Sec. 2. This is followed by a brief discussion on the various stress measures. The virtual power formulation is then applied in Sec. 4 to obtain the governing relations on the grain boundary. The free energy imbalance and the resulting reduced dissipation inequality guides the construction of the various plastic flow relations in the grain and on the grain boundary presented in Sec. 7. A brief discussion on the numerical implementation within the finite element method follows. A series of numerical examples presented in Sec. 9 serve to elucidate the theory. Conclusions are then drawn and possible extensions to the work discussed.

2 Kinematics

The finite-deformation theory of Gurtin (2008a), employed to describe the kinematic response of the grain, is briefly summarised. The main contribution of this section is the subsequent extension of the kinematics of the infinitesimal-deformation, grain-boundary theory of Gurtin (2008b) to the finite-deformation setting.

2.1 Grain

Consider a continuum body whose placement in the reference configuration is denoted $\mathcal{V}_0$ at time $t = 0$, as shown in Fig. 1. A typical material point within the reference configuration is identified by the position vector $\boldsymbol{X}$. The observed configuration of the body at a later time t is denoted $\mathcal{V}$ with a typical material point identified by the position vector $\boldsymbol{x}$. The motion $\boldsymbol{\varphi}$ relates the observed and reference configurations as $\boldsymbol{x} = \boldsymbol{\varphi}(\boldsymbol{X}, t)$. The deformation gradient is defined as the derivative of the motion $\boldsymbol{\varphi}$ with respect to the reference configuration; that is,

$$\boldsymbol{F}(\boldsymbol{X}, t) := \nabla_0 \boldsymbol{\varphi}(\boldsymbol{X}, t),$$

where $\nabla_0(\bullet) := \partial(\bullet)/\partial \boldsymbol{X}$. The Jacobian determinant of the deformation gradient is denoted by $J := \det \boldsymbol{F} > 0$ and its inverse by $j := 1/J$. The velocity is defined as the time derivative of the motion, i.e. $\boldsymbol{v} := \dot{\boldsymbol{\varphi}}$. Following the approach in the classical theory of crystal plasticity (see e.g. Lee, 1969; Rice, 1971; Hill and Rice, 1972; Asaro and Rice, 1977) the deformation gradient $\boldsymbol{F}$ is decomposed (locally) into elastic and plastic parts, denoted $\boldsymbol{F}^{\mathrm{e}}$ and $\boldsymbol{F}^{\mathrm{p}}$, respectively, as

$$\boldsymbol{F} = \boldsymbol{F}^{\mathrm{e}} \boldsymbol{F}^{\mathrm{p}}. \tag{1}$$

The multiplicative decomposition of $\boldsymbol{F}$ motivates an intermediate undistorted lattice space denoted by $\mathcal{V}_{\#}$. From micromechanical arguments $\boldsymbol{F}^{\mathrm{p}}$ is an internal variable related to dislocation flow through the crystal lattice, while $\boldsymbol{F}^{\mathrm{e}-1}$ defines the local stress-free lattice space. Plastic flow is assumed incompressible and hence $\det \boldsymbol{F}^{\mathrm{p}} = 1$ and $\det \boldsymbol{F}^{\mathrm{e}} = J$. The elastic Green–Lagrange strain tensor $\boldsymbol{E}^{\mathrm{e}}$ and the elastic right Cauchy–Green stretch tensor $\boldsymbol{C}^{\mathrm{e}}$ are defined by

$$\boldsymbol{E}^{\mathrm{e}} := \frac{1}{2}[\boldsymbol{F}^{\mathrm{e}\mathsf{T}} \boldsymbol{F}^{\mathrm{e}} - \boldsymbol{I}] = \frac{1}{2}[\boldsymbol{C}^{\mathrm{e}} - \boldsymbol{I}], \tag{2}$$

where $\boldsymbol{I}$ is the second-order material identity tensor.

As a consequence of the local multiplicative decomposition of the deformation gradient in Eq. (1), the spatial velocity gradient, denoted $\boldsymbol{l} := \nabla \boldsymbol{v} := \partial \boldsymbol{v}/\partial \boldsymbol{x}$, is additively split as follows

$$\boldsymbol{l} = \dot{\boldsymbol{F}} \boldsymbol{F}^{-1} = \underbrace{\dot{\boldsymbol{F}}^{\mathrm{e}} \boldsymbol{F}^{\mathrm{e}-1}}_{\boldsymbol{l}^{\mathrm{e}}} + \underbrace{\boldsymbol{F}^{\mathrm{e}} \boldsymbol{L}^{\mathrm{p}}_{\#} \boldsymbol{F}^{\mathrm{e}-1}}_{\boldsymbol{l}^{\mathrm{p}}}, \tag{3}$$

into the elastic and plastic (spatial) distortion rate tensors, denoted $\boldsymbol{l}^{\mathrm{e}}$ and $\boldsymbol{l}^{\mathrm{p}}$, respectively. The flow of dislocations through the crystal lattice is described kinematically via the assumption that the plastic distortion tensor in the lattice space $\boldsymbol{L}^{\mathrm{p}}_{\#}$ can be expressed in terms of the slip rates ν^{α} on the individual slip systems as

$$\boldsymbol{L}^{\mathrm{p}}_{\#} = \sum_{\alpha} \nu^{\alpha} \boldsymbol{s}^{\alpha}_{\#} \otimes \boldsymbol{m}^{\alpha}_{\#} = \sum_{\alpha} \nu^{\alpha} \mathbb{S}^{\alpha}_{\#}.$$

The notation $\sum_{\alpha}$ indicates a sum over all slip systems α. Note, the summation convention is not used for slip systems. The slip direction and slip plane normal in the lattice space for slip system α are denoted by $\boldsymbol{s}^{\alpha}_{\#}$ and $\boldsymbol{m}^{\alpha}_{\#}$, respectively. The Schmid tensor in the lattice configuration is defined by $\mathbb{S}^{\alpha}_{\#} = \boldsymbol{s}^{\alpha}_{\#} \otimes \boldsymbol{m}^{\alpha}_{\#}$. It is important to note that *the rate of plastic distortion, and not the distortion itself, plays the key role as a kinematic descriptor of plastic deformation in the finite-deformation theory.* The plastic distortion tensor in the observed configuration $\boldsymbol{l}^{\mathrm{p}}$ can be
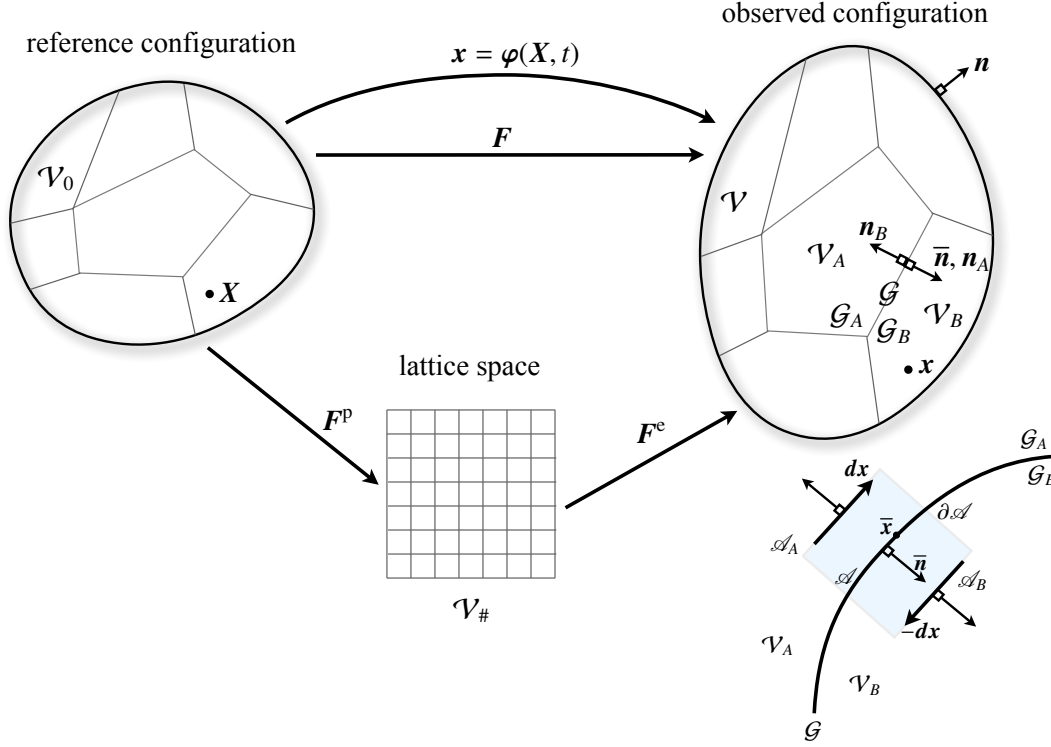
Figure 1: The continuum body in the reference and observed configurations and the associated motion φ. The undistorted lattice space $\mathcal{V}_\#$ is motivated by the multiplicative decomposition of the deformation gradient $\mathbf{F} = \mathbf{F}^e\mathbf{F}^p$. Also shown is a pill-box control volume $\mathscr{A}$ centred on the grain boundary.

obtained by a push forward of $\boldsymbol{L}_\#^p$ from the lattice space as follows

$$
\begin{aligned}
\boldsymbol{l}^p &= \boldsymbol{F}^e\boldsymbol{L}_\#^p\boldsymbol{F}^{e-1} \\
&= \sum_\alpha \nu^\alpha \underbrace{[\boldsymbol{F}^e\boldsymbol{s}_\#^\alpha]}_{\boldsymbol{s}^\alpha} \otimes \underbrace{[\boldsymbol{F}^{e\text{-T}}\boldsymbol{m}_\#^\alpha]}_{\boldsymbol{m}^\alpha} \\
&= \sum_\alpha \nu^\alpha \mathbb{S}^\alpha,
\end{aligned}
$$

where the Schmid tensor in the observed configuration is denoted by $\mathbb{S}^\alpha := \boldsymbol{s}^\alpha \otimes \boldsymbol{m}^\alpha$. It is worth noting that $\boldsymbol{s}_\#^\alpha$ and $\boldsymbol{m}_\#^\alpha$ are constant orthonormal vectors. Their counterparts in the observed configuration $\boldsymbol{s}^\alpha$ and $\boldsymbol{m}^\alpha$ are orthogonal but not necessarily unit vectors. The associated normalised spatial vectors describing slip plane α are defined by

$$
\mathbb{s}^\alpha := \frac{\boldsymbol{s}^\alpha}{|\boldsymbol{s}^\alpha|} \qquad \text{and} \qquad \mathbb{m}^\alpha := \frac{\boldsymbol{m}^\alpha}{|\boldsymbol{m}^\alpha|} .
$$

The vector $\boldsymbol{l}^\alpha$ is defined by $\boldsymbol{l}^\alpha := \boldsymbol{m}^\alpha \times \boldsymbol{s}^\alpha$. Hence $\{\boldsymbol{m}^\alpha, \boldsymbol{s}^\alpha, \boldsymbol{l}^\alpha\}$ constitutes a local orthogonal basis in the observed configuration.

Following Gurtin (2008a) the constitutive theory at the microscopic scale accounts for a continuous distribution of geometrically necessary dislocations (GNDs). The dislocations are either of edge or screw type and are characterised in terms of their Burgers and line directions as follows:

- *edge dislocation*: Burgers direction $\boldsymbol{s}_\#^\alpha$ and line direction $\boldsymbol{l}_\#^\alpha := \boldsymbol{m}_\#^\alpha \times \boldsymbol{s}_\#^\alpha$;

- *screw dislocations*: Burgers direction $\boldsymbol{s}_\#^\alpha$ and line direction $\boldsymbol{s}_\#^\alpha$.

The distributions of edge and screw dislocations are thus:

$$\underbrace{\rho_{\vdash}^{\alpha} \boldsymbol{l}_{\#}^{\alpha} \otimes \boldsymbol{s}_{\#}^{\alpha}}_{\text{edge dislocations}} \qquad \text{and} \qquad \underbrace{\rho_{\odot}^{\alpha} \boldsymbol{s}_{\#}^{\alpha} \otimes \boldsymbol{s}_{\#}^{\alpha}}_{\text{screw dislocations}},$$

where $\rho_{\vdash}^{\alpha} \in \mathbb{R}$ and $\rho_{\odot}^{\alpha} \in \mathbb{R}$ are the densities of the edge and screw dislocations, respectively. The density of the edge and screw dislocations evolve according to the relation (Gurtin, 2006):

$$\dot{\rho}_{\vdash}^{\alpha} = -\operatorname{div}\boldsymbol{q}_{\vdash}^{\alpha} + \underbrace{\nu^{\alpha}\operatorname{div}\boldsymbol{s}^{\alpha}}_{\sigma_{\vdash}^{\alpha}} = -\nabla\nu^{\alpha} \cdot \boldsymbol{s}^{\alpha} \qquad \text{and} \qquad \dot{\rho}_{\odot}^{\alpha} = -\operatorname{div}\boldsymbol{q}_{\odot}^{\alpha} + \underbrace{\nu^{\alpha}\operatorname{div}\boldsymbol{l}^{\alpha}}_{-\sigma_{\odot}^{\alpha}} = \nabla\nu^{\alpha} \cdot \boldsymbol{l}^{\alpha}. \qquad (4)$$

The vectors $\boldsymbol{q}_{\vdash}^{\alpha}$ and $\boldsymbol{q}_{\odot}^{\alpha}$ are the spatial edge and screw dislocation flux vectors respectively. Sources of edge and screw dislocations are denoted $\sigma_{\vdash}^{\alpha}$ and $\sigma_{\odot}^{\alpha}$, respectively. We note that $\boldsymbol{l}^{\alpha} = \boldsymbol{F}^{\mathrm{e}}\boldsymbol{l}_{\#}^{\alpha}$.

Following Cermelli and Gurtin (2001), the Burgers tensor in the lattice space is given by

$$\boldsymbol{G} := \boldsymbol{F}^{\mathrm{p}}\mathsf{Curl}\boldsymbol{F}^{\mathrm{p}}.$$

This result follows from performing a boundary integral of the plastic part of the deformation gradient $\boldsymbol{F}^{\mathrm{p}}$ over a closed curve in the reference configuration. Cermelli and Gurtin (2001) show that the quantity $\boldsymbol{G}^{\mathsf{T}}\boldsymbol{n}_{\#}$ provides a measure - based on the plastic strain - of the (local) Burgers vector in the lattice space – per unit area – for a plane with unit normal $\boldsymbol{n}_{\#}$. The plastically convected rate of $\boldsymbol{G}$, denoted $\overset{\square}{\boldsymbol{G}}$, can be expressed in terms of the temporal changes of the distributions of edge and screw dislocations as

$$\overset{\square}{\boldsymbol{G}} = \sum_{\alpha}[\dot{\rho}_{\vdash}^{\alpha}\boldsymbol{l}^{\alpha} \otimes \boldsymbol{s}^{\alpha} + \dot{\rho}_{\odot}^{\alpha}\boldsymbol{s}^{\alpha} \otimes \boldsymbol{s}^{\alpha}].$$

2.2 Grain Boundary

The polycrystalline body is composed of grains, separated by grain boundaries as depicted in Fig. 1. An arbitrary grain boundary in the observed configuration is denoted by $\mathcal{G}$. The grain boundary is represented as a two-sided interface, with common sides denoted by $\mathcal{G}_A$ and $\mathcal{G}_B$. The grains on either side of the grain boundary are correspondingly denoted $\mathcal{V}_A$ and $\mathcal{V}_B$. The outward unit normals to $\mathcal{G}_A$ and $\mathcal{G}_B$ are denoted $\boldsymbol{n}_A$ and $\boldsymbol{n}_B$, respectively. The normal to the grain boundary in the observed configuration is defined by $\overline{\boldsymbol{n}} := \boldsymbol{n}_A$. The evolution of the grain boundary normal with the deformation is described using the curvilinear-coordinate-based methodology presented in Javili et al. (2014). The grain boundary is assumed to be coherent (material), that is

$$\begin{aligned} \overline{\boldsymbol{\varphi}} &:= \boldsymbol{\varphi}|_{\mathcal{G}} \qquad &\text{and} \qquad &[\![\boldsymbol{\varphi}]\!] := \boldsymbol{\varphi}|_{\mathcal{G}_B} - \boldsymbol{\varphi}|_{\mathcal{G}_A} = \boldsymbol{0} \\ \overline{\boldsymbol{v}} &:= \dot{\overline{\boldsymbol{\varphi}}} := \boldsymbol{v}|_{\mathcal{G}} \qquad &\text{and} \qquad &[\![\boldsymbol{v}]\!] = \boldsymbol{0}. \end{aligned} \qquad (5)$$

In the spirit of Gurtin (2008b) for the infinitesimal-deformation theory, the intra-grain interaction and inter-grain interaction moduli are defined in terms of the normalized slip plane directions and normals as

$$\overline{\mathbb{C}}_{IJ}^{\alpha\beta} = [\mathbb{s}_I^{\alpha} \cdot \mathbb{s}_J^{\beta}][\mathbb{m}_I^{\alpha} \times \overline{\boldsymbol{n}}] \cdot [\mathbb{m}_J^{\beta} \times \overline{\boldsymbol{n}}]. \qquad (6)$$

The slip interaction moduli are classified as follows:

- $\overline{\mathbb{C}}_{AA}^{\alpha\beta}$: *intra-grain* interaction moduli for grain A;

- $\overline{\mathbb{C}}_{AB}^{\alpha\beta}$: *inter-grain* interaction moduli between grains A and B;

- $\overline{\mathbb{C}}_{BB}^{\alpha\beta}$: *intra-grain* interaction moduli for grain B.

The inter-grain interaction moduli for an arbitrary pair of slip systems and grain-boundary orientation thus have the range $-1 \leq \overline{\mathbb{C}}_{AB}^{\alpha\beta} \leq 1$. The inter-grain interaction moduli characterise the interaction between slips systems in adjacent grains separated by a grain boundary. The systems are *non-interactive* if $\overline{\mathbb{C}}_{AB}^{\alpha\beta} = 0$ and *maximally interactive* if $|\overline{\mathbb{C}}_{AB}^{\alpha\beta}| = 1$. These definitions imply that a pair of slips systems in adjacent grains are (see Eq. (6)):

- *non-interactive* if and only if either

$$\mathrm{s}_A^\alpha \cdot \mathrm{s}_B^\beta = 0 \qquad\qquad \text{or} \qquad\qquad [\mathrm{m}_A^\alpha \times \overline{\boldsymbol{n}}] \cdot [\mathrm{m}_B^\beta \times \overline{\boldsymbol{n}}] = 0\,;$$

- *maximally interactive* if and only if all of the following conditions are satisfied

$$\mathrm{s}_A^\alpha = \pm \mathrm{s}_B^\alpha\,, \qquad\qquad \mathrm{m}_A^\alpha \cdot \overline{\boldsymbol{n}} = 0\,, \qquad\qquad \mathrm{m}_B^\beta \cdot \overline{\boldsymbol{n}} = 0\,.$$

The boundary integral of the plastic distortion tensor $\boldsymbol{l}^{\mathrm{p}}$ over a closed loop $\mathscr{C}$ in the observed configuration,

$$\int_{\mathscr{C}} \boldsymbol{l}^{\mathrm{p}} d\boldsymbol{x} = \sum_\alpha \int_{\mathscr{C}} \nu^\alpha [\boldsymbol{s}^\alpha \otimes \boldsymbol{m}^\alpha] d\boldsymbol{x}\,,$$

is the measure proposed to characterise the defect structure at the grain boundary. Integration over a pill box $\mathscr{A}$ centered on the grain boundary as depicted in Fig. 1 yields

$$\int_{\mathscr{C}} \boldsymbol{l}^{\mathrm{p}} d\boldsymbol{x} = \sum_\alpha [\nu_A^\alpha [\boldsymbol{s}_A^\alpha \otimes \boldsymbol{m}_A^\alpha] d\boldsymbol{x} - \nu_B^\alpha [\boldsymbol{s}_B^\alpha \otimes \boldsymbol{m}_B^\alpha] d\boldsymbol{x}]$$
$$= -\sum_\alpha [\![\nu^\alpha [\boldsymbol{s}^\alpha \otimes \boldsymbol{m}^\alpha]]\!] d\boldsymbol{x}\,.$$

Using the property that the line segement $d\boldsymbol{x}$ is tangent to the grain boundary, this expression can be written as

$$-\sum_\alpha [\![\nu^\alpha [\boldsymbol{s}^\alpha \otimes \boldsymbol{m}^\alpha]]\!][\boldsymbol{i} - \overline{\boldsymbol{n}} \otimes \overline{\boldsymbol{n}}] d\boldsymbol{x} = \underbrace{[\![\boldsymbol{l}^{\mathrm{p}}]\!][\overline{\boldsymbol{n}}\times]}_{\dot{\overline{\mathbb{H}}}}[\overline{\boldsymbol{n}} \times d\boldsymbol{x}]\,,$$

where $[\boldsymbol{n}\times]_{ij} := \epsilon_{ikj} n_k$. The term $[\overline{\boldsymbol{n}} \times d\boldsymbol{x}]$ is an area element directed orthogonal to the pill box and tangent to the grain boundary. Hence $\dot{\overline{\mathbb{H}}}$ provides a rate-like measure of the kinematic and geometric mismatch at the grain boundary. The measure $\overline{\mathbb{H}}$ is defined by

$$\overline{\mathbb{H}} = \int_0^t \dot{\overline{\mathbb{H}}}\, dt\,.$$

The Schmidt orientation tensor for slip system α in grain J, denoted $\overline{\mathbb{N}}_J^\alpha$, is defined by

$$\sum_\alpha \left[\nu_B^\alpha \overline{\mathbb{N}}_B^\alpha - \nu_A^\alpha \overline{\mathbb{N}}_A^\alpha\right] = \dot{\overline{\mathbb{H}}}\,,$$

where

$$\overline{\mathbb{N}}_J^\alpha = \mathbb{S}_J^\alpha [\overline{\boldsymbol{n}}\times] = \boldsymbol{s}_J^\alpha \otimes [\boldsymbol{m}_J^\alpha \times \overline{\boldsymbol{n}}] \qquad\qquad \text{for } J = A, B\,.$$

Remark

For the infinitesimal theory, following a near-identical procedure to that outlined above, the grain boundary Burgers tensor (not the rate thereof) is given by:

$$\overline{\mathbb{H}}^{\mathrm{lin}} = [\![\boldsymbol{H}^{\mathrm{p}}]\!][\overline{\boldsymbol{n}}\times]\,,$$

where $\boldsymbol{H}^{\mathrm{p}} = \sum_\alpha \gamma^\alpha \mathbb{S}^\alpha$ and $\gamma^\alpha = \int_0^t \nu^\alpha\, dt$.

2.3 Alternative Measure of Mismatch

As shown in Gottschalk et al. (2015) for the infinitesimal-deformation theory, the rate of change of the grain boundary Burgers tensor $\overline{\mathbb{H}}^{\mathrm{lin}}$ can be zero for non-zero slip rates at the grain boundary for misorientated grains. This can result in zero dissipation for a finite slip rate as discussed in detail in Sec. 6.2. An alternative measure of mismatch, which ensures finite dissipation for finite slip rates, was proposed in Gottschalk et al. (2015). The

measure entails a sum over all slip systems from both sides of the grain boundary for the slip systems with the least mismatch. This implies that resistance to dislocation flow on a slip system at the grain boundary depends on the geometrically most favourable interaction partner in the adjacent grain. The extension of this mismatch measure to finite deformations is given by

$$\dot{\overline{\mathbb{H}}}_R^{\alpha\beta} := \sqrt{R^{\alpha\beta}}[\nu_B^\beta \overline{\mathbb{N}}_B^\beta - \nu_A^\alpha \overline{\mathbb{N}}_A^\alpha] \,.$$

The flag $R^{\alpha\beta}$ take the values 1 or 0, in this way allowing a selection of particular combinations of slip systems for the two adjacent grains. The square root is introduced to arrive at a convenient formulation for the magnitude, given by

$$\left|\dot{\overline{\mathbb{H}}}_R^{\alpha\beta}\right|^2 = R^{\alpha\beta}\left|\nu_B^\beta \overline{\mathbb{N}}_B^\beta - \nu_A^\alpha \overline{\mathbb{N}}_A^\alpha\right|^2 \,.$$

3 Kinetics

In the spirit of the theory of surface elasticity proposed by Gurtin and Murdoch (1975), the grain and the grain boundary are endowed with their own free energies. In the case of the grain boundary, the free energy is solely a defect energy, that is, there is no energetic stress measure (macroscopic or microscopic) on the grain boundary.

The macroscopic tensorial Cauchy stress in the grain is denoted by $\boldsymbol{\sigma}$. Scalar and vector microscopic forces on each of the slip systems, denoted by π^α and $\boldsymbol{\xi}^\alpha$ respectively, are postulated as conjugates to the slip rates ν^α and their spatial gradients $\nabla\nu^\alpha$. The vectorial microscopic stresses exist only in the grain. Scalar microscopic forces conjugate to the slip rates on either side of the grain boundary are denoted by $\overline{\pi}_A^\alpha$ and $\overline{\pi}_B^\alpha$. The power conjugate pairings are thus as follows:

$$
\begin{array}{lll}
\boldsymbol{\sigma} \leftrightarrow \boldsymbol{l}^{\mathrm{e}} & \text{Cauchy stress} & \text{in } \mathcal{V}\,, \\
\pi^\alpha \leftrightarrow \nu^\alpha & \text{scalar microscopic force} & \text{in } \mathcal{V}\,, \\
\boldsymbol{\xi}^\alpha \leftrightarrow \nabla\nu^\alpha & \text{vector microscopic force} & \text{in } \mathcal{V}\,, \\
\overline{\pi}_A^\alpha \leftrightarrow \nu_A^\alpha\,, \overline{\pi}_B^\alpha \leftrightarrow \nu_B^\alpha & \text{scalar microscopic forces} & \text{on } \mathcal{G}_A, \mathcal{G}_B\,.
\end{array}
$$

The primary difference between the geometrically linear power conjugate parings and the proposed nonlinear ones is the use of slip rates as primal quantities. The primal quantities in the linear theory are the rates themselves.

The lattice stress $\boldsymbol{T}_\#^{\mathrm{e}}$ is defined so as to be power conjugate to the rate of the elastic strain $\dot{\boldsymbol{E}}^{\mathrm{e}}$ and is defined via the relation:

$$\boldsymbol{\sigma} : \boldsymbol{l}^{\mathrm{e}} = \boldsymbol{\sigma} : [\dot{\boldsymbol{F}}^{\mathrm{e}\mathsf{T}}\boldsymbol{F}^{\mathrm{e}-1}] = [\boldsymbol{F}^{\mathrm{e}-1}\boldsymbol{\sigma}\cdot\boldsymbol{F}^{\mathrm{e}-\mathsf{t}}] : [\boldsymbol{F}^{\mathrm{e}-\mathsf{t}}\dot{\boldsymbol{F}}^{\mathrm{e}\mathsf{T}}] = j\boldsymbol{T}_\#^{\mathrm{e}} : \dot{\boldsymbol{E}}^{\mathrm{e}} \,.$$

4 Virtual Power Formulation

The virtual power formulation is employed to determine the governing equations in the grain and on the grain boundary for the finite-deformation setting. The governing relations in the grain follow directly from Gurtin (2008a) and are therefore simply stated without derivation. The governing relations on the grain boundary are new and details of the derivation are given. Virtual rate-like quantities are denoted by $\delta(\bullet)$.

4.1 Grain

The classical equilibrium equation in the grain and the Cauchy traction vector $\boldsymbol{t}$, obtained using the virtual power balance, are given by

$$\mathrm{div}\boldsymbol{\sigma} + \boldsymbol{b} = \boldsymbol{0} \quad \text{in } \mathcal{V} \qquad \text{and} \qquad \boldsymbol{t}(\boldsymbol{n}) = \boldsymbol{\sigma}\boldsymbol{n} \quad \text{on } \partial\mathcal{V}\,, \tag{7}$$

there the body force vector per unit observed volume is denoted here by $\boldsymbol{b}$.

The microscopic force balance and the scalar microscopic traction Ξ^α are given by

$$\operatorname{div}\boldsymbol{\xi}^\alpha + \tau^\alpha - \pi^\alpha = 0 \quad \text{in } \mathcal{V} \qquad \text{and} \qquad \Xi^\alpha(\boldsymbol{n}) = \boldsymbol{\xi}^\alpha \cdot \boldsymbol{n} \quad \text{on } \partial\mathcal{V}, \tag{8}$$

where resolved shear stress on slip system α is denoted by $\tau^\alpha := \boldsymbol{\sigma} : \mathbb{S}^\alpha$. A prescribed scalar microscopic traction Ξ^α of zero is termed a micro-free boundary condition. A homogeneous Dirichlet boundary condition for the slip rate $\nu^\alpha = 0$ is term micro-hard. A micro-hard condition is often assumed to hold on the grain boundary.

The macrscopic and microscopic balances, (7) and (8), are coupled via the Cauchy stress and the resolved shear stress, and the plastic flow relation to be derived in Sec. 7.1.

4.2 Grain Boundary

Consider, once again, a two-sided "pillbox" control region $\mathscr{A}$ centred on the grain boundary $\mathcal{G}$. The two sides of the the pillbox are denoted $\mathscr{A}_A$ and $\mathscr{A}_B$, with outward unit normals respectively denoted by $-\boldsymbol{n}_A$ and $-\boldsymbol{n}_B$. As mentioned previously, no vectorial microforces exist within the grain boundary. The scalar microscopic forces $\overline{\pi}_A^\alpha$ and $\overline{\pi}_B^\alpha$ do however exist on either side of the two-sided grain boundary.

The balance of internal and external virtual power, denoted $\overline{P}_{\text{int}}$ and $\overline{P}_{\text{ext}}$ respectively, for the grain boundary reads:

$$\underbrace{\int_{\mathscr{A}_A} [\boldsymbol{\sigma}_A \overline{\boldsymbol{n}}_A] \cdot \delta\overline{\boldsymbol{v}}\, \mathrm{d}a + \int_{\mathscr{A}_B} [\boldsymbol{\sigma}_B \overline{\boldsymbol{n}}_B] \cdot \delta\overline{\boldsymbol{v}}\, \mathrm{d}a + \sum_\alpha \int_{\mathscr{A}} [\overline{\pi}_A^\alpha \delta\nu_A^\alpha + \overline{\pi}_B^\alpha \delta\nu_B^\alpha]\, \mathrm{d}a}_{\overline{P}_{\text{int}}}$$

$$= \underbrace{\sum_\alpha \int_{\mathscr{A}_A} [-\boldsymbol{\xi}_A^\alpha \cdot \overline{\boldsymbol{n}}_A] \delta\nu_A^\alpha\, \mathrm{d}a + \sum_\alpha \int_{\mathscr{A}_B} [\boldsymbol{\xi}_B^\alpha \cdot \overline{\boldsymbol{n}}_B] \delta\nu_B^\alpha\, \mathrm{d}a}_{\overline{P}_{\text{ext}}}. \tag{9}$$

Setting $\delta v_J^\alpha = 0$ gives the standard traction continuity condition for coherent (material) grain boundaries (interfaces):

$$[\![\boldsymbol{\sigma}]\!]\overline{\boldsymbol{n}} = \boldsymbol{0}.$$

Now set $\delta\overline{\mathbf{v}} \equiv \boldsymbol{0}$. The virtual power balance yields the two microscopic force balance (one for each side) on the grain boundary as

$$0 = \sum_\alpha \int_{\mathscr{A}_A} [-\overline{\pi}_A^\alpha + \boldsymbol{\xi}_A^\alpha \cdot \overline{\boldsymbol{n}}_A]\, \delta\nu_A^\alpha \mathrm{d}a + \sum_\alpha \int_{\mathscr{A}_B} [-\overline{\pi}_B^\alpha + \boldsymbol{\xi}_B^\alpha \cdot \overline{\boldsymbol{n}}_B]\, \delta\nu_B^\alpha \mathrm{d}a$$

$$= \sum_\alpha \int_{\mathscr{A}} [-\overline{\pi}_A^\alpha - \boldsymbol{\xi}_A^\alpha \cdot \overline{\boldsymbol{n}}] \delta\nu_A^\alpha \mathrm{d}a + \sum_\alpha \int_{\mathscr{A}} [-\overline{\pi}_B^\alpha + \boldsymbol{\xi}_B^\alpha \cdot \overline{\boldsymbol{n}}]\, \delta\nu_B^\alpha \mathrm{d}a$$

$$\implies \quad -\overline{\pi}_A^\alpha - \boldsymbol{\xi}_A^\alpha \cdot \overline{\boldsymbol{n}} = 0 \quad \text{on } \mathcal{G}_A \qquad \text{and} \qquad -\overline{\pi}_B^\alpha + \boldsymbol{\xi}_B^\alpha \cdot \overline{\boldsymbol{n}} = 0 \quad \text{on } \mathcal{G}_B. \tag{10}$$

The microforce balances on the grain boundary (10) are coupled to the response in the grains on either side via the resolved shear stress and the scalar microscopic traction.

5 Free Energy Imbalance

The free energy per unit volume of the grain in the lattice space is denoted by Ψ. The free energy, measured per unit area, of the grain boundary in the lattice space is denoted by $\overline{\Psi}$. The non-negative dissipation density, measured per unit volume of the observed configuration, is denoted by $\mathcal{D}$. Similarly, the dissipation per unit observed area of the grain boundary is denoted by $\overline{\mathcal{D}} \geq 0$. The free energy imbalance imposes the physical restriction that the rate of change of free energy is not greater than the external power expended.

5.1 Grain

Following Gurtin (2008a) the localised free energy imbalance in the grain takes the form:

$$0 \leq \mathcal{D} = -\dot{\Psi} j + \boldsymbol{\sigma} : \boldsymbol{l}^{\mathrm{e}} + \sum_{\alpha} \left[\pi^{\alpha} \nu^{\alpha} + \boldsymbol{\xi}^{\alpha} \cdot \nabla \nu^{\alpha} \right]$$

$$= -\dot{\Psi} j + j \boldsymbol{T}_{\#}^{\mathrm{e}} : \dot{\boldsymbol{E}}^{\mathrm{e}} + \sum_{\alpha} \left[\pi^{\alpha} \nu^{\alpha} + \boldsymbol{\xi}^{\alpha} \cdot \nabla \nu^{\alpha} \right]. \tag{11}$$

5.2 Grain Boundary

Following a similar procedure as for the grain and using the external power in the grain boundary, defined in Eq. (9), the free energy imbalance on the grain boundary takes the form:

$$0 = \overline{\int_{\mathscr{A}} \overline{\Psi} \, \overline{j} \, \mathrm{d}a} - \overline{P}_{\mathrm{ext}} + \int_{\mathscr{A}} \overline{\mathcal{D}} \, \mathrm{d}a$$

$$= \int_{\mathscr{A}} \dot{\overline{\Psi}} \, \overline{j} \, \mathrm{d}a - \sum_{\alpha} \int_{\mathscr{A}} \left[\overline{\pi}_A^{\alpha} \nu_A^{\alpha} + \overline{\pi}_B^{\alpha} \nu_B^{\alpha} \right] \mathrm{d}a + \int_{\mathscr{A}} \overline{\mathcal{D}} \, \mathrm{d}a$$

$$\implies \quad 0 \leq \overline{\mathcal{D}} = -\dot{\overline{\Psi}} \, \overline{j} + \sum_{\alpha} \left[\overline{\pi}_A^{\alpha} \nu_A^{\alpha} + \overline{\pi}_B^{\alpha} \nu_B^{\alpha} \right].$$

The contribution of the product of the scalar microscopic forces and the slip rates on either side of the grain boundary will play a key role in subsequent developments.

6 Reduced Dissipation Inequalities and the Elastic Constitutive Relations

The constitutive relations are obtained by endowing the free energy functions in the various parts of the body with structure. A set of (arbitrary) properties associated with all slip systems is denoted as follows

$$\vec{\rho} := \left\{ \rho^1, \rho^2, \ldots, \rho^{\alpha}, \ldots, \rho^{n_{\mathrm{ss}}} \right\},$$

where n_{ss} is the number of slip systems.

6.1 Grain

Assume a free energy for the grain decoupled into an elastic (macroscopic) and a defect (microscopic) part, denoted Ψ^{e} and Ψ^{d} respectively, that takes the form

$$\Psi = \Psi^{\mathrm{e}}(\boldsymbol{E}^e) + \Psi^{\mathrm{d}}(\vec{\rho}).$$

The defect energy Ψ^{d} is defined to be a function of the dislocation densities. The scalar energetic defect forces associated with edge and screw dislocations are respectively defined by

$$f_{\vdash}^{\alpha} = j \frac{\partial \Psi^{\mathrm{d}}(\vec{\rho})}{\partial \rho_{\vdash}^{\alpha}} \qquad \text{and} \qquad f_{\odot}^{\alpha} = j \frac{\partial \Psi^{\mathrm{d}}(\vec{\rho})}{\partial \rho_{\odot}^{\alpha}}.$$

Making use of Eq. (4), the time rate of change of the defect energy yields the following definition for the energetic vectorial microstress $\boldsymbol{\xi}_{\mathrm{en}}^{\alpha}$:

$$j \dot{\Psi}^{\mathrm{d}}(\vec{\rho}) = \sum_{\alpha} \left[f_{\vdash}^{\alpha} \dot{\rho}_{\vdash}^{\alpha} + f_{\odot}^{\alpha} \dot{\rho}_{\odot}^{\alpha} \right]$$

$$= \sum_{\alpha} \underbrace{\left[-f_{\vdash}^{\alpha} \boldsymbol{s}^{\alpha} + f_{\odot}^{\alpha} \boldsymbol{l}^{\alpha} \right]}_{\boldsymbol{\xi}_{\mathrm{en}}^{\alpha}} \cdot \nabla \nu^{\alpha}.$$

Using these relations and definitions, the free energy imbalance in the grain (11) yields the constitutive relation for the lattice stress $\boldsymbol{T}_{\#}^{\mathrm{e}}$ and what remains is the reduced dissipation in the grain $\mathcal{D}^{\mathrm{red}}$ obtained as follows:

$$\mathcal{D} = -j \left[\frac{\partial \Psi^{\mathrm{e}}}{\partial \boldsymbol{E}^{\mathrm{e}}} : \dot{\boldsymbol{E}}^{\mathrm{e}} + \dot{\Psi}^{\mathrm{d}} \right] + j \boldsymbol{T}_{\#}^{\mathrm{e}} : \dot{\boldsymbol{E}}^{\mathrm{e}} + \sum_\alpha [\pi^\alpha \nu^\alpha + \boldsymbol{\xi}^\alpha \cdot \nabla \nu^\alpha] \geq 0$$

$$\implies \quad \boldsymbol{T}_{\#}^{\mathrm{e}} = \frac{\partial \Psi^{\mathrm{e}}}{\partial \boldsymbol{E}^{\mathrm{e}}}, \tag{12}$$

$$\mathcal{D}^{\mathrm{red}} := \sum_\alpha \left[\underbrace{[\boldsymbol{\xi}^\alpha - \boldsymbol{\xi}_{\mathrm{en}}^\alpha]}_{\boldsymbol{\xi}_{\mathrm{dis}}^\alpha} \cdot \nabla \nu^\alpha + \pi^\alpha \nu^\alpha \right] \geq 0,$$

where $\boldsymbol{\xi}_{\mathrm{dis}}^\alpha$ is the dissipative vectorial microstress. The scalar microstress π^α is assumed to be fully dissipative. To elucidate the role of the grain boundary, the vectorial microstress is assumed to be fully energetic. That is, we assume the following:

$$\boldsymbol{\xi}_{\mathrm{dis}}^\alpha \equiv \boldsymbol{0} \qquad \implies \qquad \boldsymbol{\xi}^\alpha \equiv \boldsymbol{\xi}_{\mathrm{en}}^\alpha$$
$$\pi_{\mathrm{en}}^\alpha \equiv 0 \qquad \implies \qquad \pi^\alpha \equiv \pi_{\mathrm{dis}}^\alpha$$

and hence the reduced dissipation inequality in the grain simplifies further as

$$\mathcal{D}^{\mathrm{red}} \equiv \sum_\alpha \pi_{\mathrm{dis}}^\alpha \nu^\alpha \geq 0. \tag{13}$$

6.2 Grain Boundary

The grain boundary is assumed from the onset to be fully dissipative. Following Gurtin and Needleman (2005); Gurtin (2008b), the reduced dissipation on the grain boundary is expressed in terms of the rate of change of the defect measure on the grain boundary $\dot{\overline{\mathbb{H}}}$ and its conjugate kinetic quantity $\overline{\boldsymbol{K}}$, or equivalently the sum of the dissipation from each slip system on either side of the grain boundary $\overline{\pi}_{J,\mathrm{dis}}^\alpha \nu_J^\alpha$. The reduced dissipation inequality can also be expressed in a form that is amenable to the the alternative measure of mismatch at the grain boundary proposed in Sec. 2.3. That is,

$$\overline{\mathcal{D}}^{\mathrm{red}} = \underbrace{\overline{\boldsymbol{K}} : \dot{\overline{\mathbb{H}}}}_{(I)} = \underbrace{\sum_\alpha [\overline{\pi}_{A,\mathrm{dis}}^\alpha \nu_A^\alpha + \overline{\pi}_{A,\mathrm{dis}}^\alpha \nu_B^\alpha]}_{(II)} = \underbrace{\sum_{\alpha,\beta} \overline{\boldsymbol{K}}^{\alpha\beta} : \dot{\overline{\mathbb{H}}}_R^{\alpha\beta}}_{(III)} \geq 0, \tag{14}$$

where $\overline{\boldsymbol{K}}^{\alpha\beta}$ is the conjugate kinetic quantity to $\dot{\overline{\mathbb{H}}}^{\alpha\beta}$.

7 Plastic Flow Relations

In order to complete the theory, the reduced dissipation inequalities in the various parts of the body (13, 14) are satisfied in a thermodynamically consistent manner by postulating plastic flow relations for the dissipative internal variables. We restrict attention here to viscoplastic flow relations to circumvent well-documented problems associated with the rate-independent theory.

7.1 Grain

A regularized effective dissipation function for the grain, denoted by D_{vis}^α, is proposed and takes the form:

$$D_{\mathrm{vis}}^\alpha = \frac{S}{m+1} \left[\frac{|\nu^\alpha|}{\nu_0} \right]^{m+1} \nu_0,$$

where $S > 0$ is the slip resistance (assumed constant), ν_0 is the reference value for the slip rate and $m > 0$ is the rate sensitivity. The scalar microforce follows as:

$$\pi_{\mathrm{dis}}^\alpha = \frac{\partial D_{\mathrm{vis}}^\alpha}{\partial \nu^\alpha} = S \left[\frac{|\nu^\alpha|}{\nu_0} \right]^m \mathrm{sgn}\nu^\alpha \, .$$

It is clear that this regularized result for $\pi_{\mathrm{dis}}^\alpha$ satisfies the reduced dissipation inequality in the grain (13).

7.2 Grain Boundary

Viscous plastic flow relations on the grain boundary are constructed so as to mimic those in the bulk. The reduced dissipation inequality on the grain boundary (14) can be satisfied in a variety of ways. The first two possibilities discussed here were proposed by Gurtin (2008a) for the infinitesimal-deformation problem and are hence referred to as the Gurtin I and Gurtin II models. The third option is termed the modified formulation and attempts to address various limitations of the Gurtin theory as detailed in Gottschalk et al. (2015).

7.2.1 Plastic flow relations in terms of $\dot{\overline{\mathbb{H}}}$: the Gurtin I model

In the Gurtin I model, the plastic flow relation is chosen so as to ensure that the term labelled I in the reduced dissipation inequality (14) is satisfied. Thus a regularized dissipation potential for the grain boundary is selected as follows:

$$\overline{D}_{\mathrm{vis}} = \frac{\overline{S}}{\overline{m} + 1} \left[\frac{|\dot{\overline{\mathbb{H}}}|}{\dot{\overline{\mathbb{H}}}_0} \right]^{\overline{m}+1} \dot{\overline{\mathbb{H}}}_0 \, , \tag{15}$$

where $\overline{S} > 0$ is the (constant) slip resistance, $\dot{\overline{\mathbb{H}}}_0$ is the reference scalar value for the rate of the grain-boundary Burgers tensor and $\overline{m} > 0$ is the rate sensitivity parameter. The flow relation for $\overline{K}$ follows as

$$\overline{K} = \frac{\partial \overline{D}_{\mathrm{vis}}}{\partial \dot{\overline{\mathbb{H}}}} = \overline{S}_0 \left[\frac{|\dot{\overline{\mathbb{H}}}|}{\dot{\overline{\mathbb{H}}}_0} \right]^{\overline{m}} \frac{\dot{\overline{\mathbb{H}}}}{|\dot{\overline{\mathbb{H}}}|} \, . \tag{16}$$

7.2.2 Flow relations in term of ν^α: the Gurtin II model

In the Gurtin II model, the plastic flow relations are chosen so as to ensure that each term within the summation term (labelled II in the reduced dissipation inequality) is satisfied separately.

A regularized dissipation potential for side I of the grain boundary is chosen as

$$\overline{D}_{\mathrm{vis},I}^\alpha = \frac{\overline{S}}{\overline{m} + 1} \left[\frac{|\nu_I^\alpha|}{\nu_0} \right]^{\overline{m}+1} \nu_0 \, ,$$

where ν_0 is the reference value for the rate of the grain-boundary slip, and the remaining parameters are defined as in Eq. (15). The regularized dissipation function for the grain boundary follows as

$$\overline{D}_{\mathrm{vis}}^\gamma = \sum_\alpha \left[\overline{D}_{\mathrm{vis},A}^\alpha + \overline{D}_{\mathrm{vis},B}^\alpha \right] \, .$$

The dissipative internal microscopic forces on either side of the grain boundary (see Eq. (10)) are thus obtained as

$$\pi_{I,\mathrm{dis}}^\alpha = \frac{\partial \overline{D}_{\mathrm{vis}}^\gamma}{\partial \nu_I^\alpha} = \overline{S} \left[\frac{|\nu_I^\alpha|}{\nu_0} \right]^{\overline{m}} \frac{\nu_I^\alpha}{|\nu_I^\alpha|} \, .$$

7.2.3 Flow relations in term of $\dot{\overline{\mathbb{H}}}_R^{\alpha\beta}$: the modified model

In the modified model, the plastic flow relation is chosen so as to ensure that each term within the summation term (labelled III in the reduced dissipation inequality) is satisfied separately. The regularized dissipation potential for the modified model is chosen to be

$$\overline{D}_{\text{vis,R}} = \frac{\overline{S}}{\overline{m}+1}\left[\frac{|\dot{\overline{\mathbb{H}}}_R|}{\dot{\overline{\mathbb{H}}}_0}\right]^{m+1}\dot{\overline{\mathbb{H}}}_0$$

where

$$|\dot{\overline{\mathbb{H}}}| := \sqrt{\sum_\alpha \sum_\beta |\dot{\overline{\mathbb{H}}}_R^{\alpha\beta}|^2}.$$

8 Finite Element Approximation

The non-linear coupled system of equations governing the response of the grain and the grain boundary are solved approximately using the finite element method in space in conjunction with a Newton–Raphson procedure. Rate quantities are approximated using the finite difference method. Equation 4 for the evolution of the density of the edge and screw dislocations is approximated using a backward-Euler scheme. The evolution of the elastic constitutive relation (12) requires an approximation of $\boldsymbol{F}^{\text{p}}$ (see Eq. (2)). A Crank–Nicholson interpolation of the exponential approximation for $\dot{\boldsymbol{F}}^{\text{p}}$ proposed by Steinmann and Stein (1996) is employed to ensure that the plastic incompressibility constraint is fulfilled. The incremental form of the system of governing equation is recast into a variational format following a similar procedure as in Gottschalk et al. (2015) for the infinitesimal deformation problem.

The incremental variational problem is solved approximately using the finite element method. The finite element library AceGen (Korelc, 2002) is used to implement the solution scheme. This allows the system of residual equations and the numerical tangent to be computed directly from the incremental potential arising in the variational problem. A time-step duration control procedure is used to optimise the time-step size and to ensure quadratic convergence of the Newton–Raphson scheme. The grain is discretized using Lagrangian $Q1$ elements. The nodal degrees of freedom are $(\boldsymbol{u}, \vec{\nu})$. The grain boundary is also approximated using $Q1$ elements with negligible thickness in the direction of the grain boundary normal. The evaluation and integration of quantities on the grain boundary are performed with respect to the mid-plane of the grain-boundary element. The kinematic coherence condition (5) is enforced using a penalty formulation described in Gottschalk et al. (2015).

9 Numerical Examples

The grain-boundary model developed in the preceding sections is elucidated via a series of three-dimensional numerical examples. A detailed numerical investigation of the infinitesimal-deformation theory was presented in Gottschalk et al. (2015). The influence of lattice misorientation and the grain boundary orientation on the overall response of the specimen was demonstrated for single and double slip bi-crystals, and for a face-centred cubic (FCC) crystal composed of multiple grains. The objectives here are to compare the infinitesimal- and finite-deformation theories, to illustrate features of the finite-deformation theory, and to compare the influence of the various different defect measures proposed to describe the kinematic mismatch at the grain boundary on the overall response.

The first numerical example problem is of torsion in a single slip system bi-crystal. The tensile response of a double slip system polycrystal is then examined. The final example investigates the role of the grain boundary for nano-indentation of a FCC bi-crystal and is inspired by the experiments of Britton et al. (2009).

The elastic response is governed by a standard neo-Hookean free energy (see e.g. Holzapfel, 2000). The constitutive parameters used, unless specified otherwise, are listed in Table 1. The computations are simplified by choosing a linear viscous relation. A more realistic range of viscous parameters will be explored in future work.

Table 1: Constitutive parameters used for the numerical examples unless stated otherwise. See Gottschalk et al. (2015) for further details and definitions.

First Lamé parameter	λ	1.05×10^{-1}	N/µm^2
Second Lamé parameter	μ	5.4×10^{-2}	N/µm^2
Burgers vector length	b	2.5×10^{-4}	µm
Back stress cut-off radius	R	2×10^{-2}	µm
Reference slip rate	ν_0	1	/s
	$\dot{\mathbb{H}}_0$	1	/s
Slip resistance	S	1	N/µm^2
	$\overline{S}$	1×10^{-1}	N/µm^2
Rate sensitivity	$m, \overline{m}$	1	

9.1 Torsion of a Bi-crystal

Consider the $100 \times 100 \times 400$ µm bi-crystal shown in Fig. 2. Single slip is assumed for both grains. The orientation of the slip systems and the grain boundary in the reference configuration is shown in Fig. 2(b). The crystal lattice in grains A and B is defined by $(\boldsymbol{s}_A, \boldsymbol{m}_A) = (1/\sqrt{2})((1,1,0),(1,-1,0))$ and $(\boldsymbol{s}_B, \boldsymbol{m}_B) = ((1,0,0),(0,-1,0))$, respectively. The grain boundary normal vector is given by $\overline{\boldsymbol{n}} = \boldsymbol{e}_3$ in the reference configuration. The slip directions are chosen parallel to the grain boundary to minimise the role of the grain boundary. As shown in Fig. 2(a), each grain is discretized into $20 \times 20 \times 20$ elements. The lower face of grain A is fully fixed and micro-hard conditions imposed. A rotation in the $\boldsymbol{e}_1-\boldsymbol{e}_2$ plane is prescribed on the upper face and micro-hard conditions assumed. The finite rotation is applied in 36 equal load increments. The Gurtin I and II models were used for this example. For this problem and geometry, the predictions of the two models are indistinguishable.
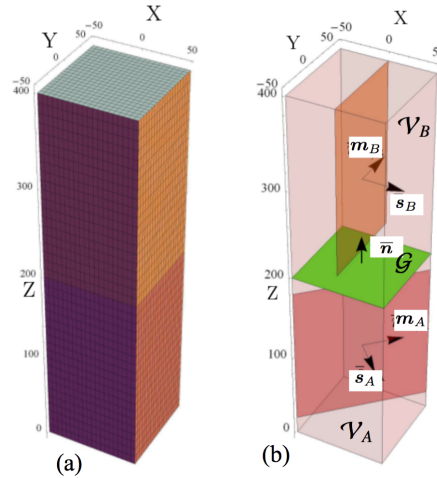

Figure 2: The problem of torsion in a bi-crystal.

The deformed states predicted using the infinitesimal- and finite-deformation theory for a twist of $\phi_3 = \pi/5$ are shown in Fig. 3. The $\boldsymbol{e}_3$ component of the displacement field and the slip are superimposed upon the domain. The relation between the resulting component of the torque vector in the $\boldsymbol{e}_3$ direction on the upper face, defined by $M_z := |\int \overline{\boldsymbol{x}} \times \boldsymbol{\sigma} \boldsymbol{e}_3 \, \mathrm{d}A|$, where $\overline{\boldsymbol{x}}$ is a point on the upper face, and the angle of twist ϕ_3 is shown in Fig. 4. The infinitesimal- and finite-deformation models are in good agreement for ϕ_3 approximately less than 0.1 rad. This is to be expected as the deformations are reasonably small within this range. For $\phi_3 > 0.1$ rad the disagreement between the models becomes significant with the infinitesimal-deformation model exhibiting a far stiffer response. In the infinitesimal-deformation model, the deformation is concentrated near the upper surface of grain B as shown in Fig. 3(a). This is non-physical. The response of the finite-deformation model is far smoother as shown in Fig. 3(b). Interpenetration occurs in the infinitesimal-deformation model when the twist is greater than approximately 0.2π rad. It is clear from the distribution of the slip that the infinitesimal-deformation model is unable to account for the change in the interaction of the slip systems with deformation. The finite-deformation model captures the deformation-induced transformation of the adjacent slip systems to non-parallel.

The finite-deformation model can predict the response of the system for far greater twists, as shown in Fig. 5 for $\phi_3 \in [0, 2\pi]$. The change in the grain-boundary interaction coefficient $\overline{\mathbb{C}}_{AB}$ from the beginning to the end of the loading cycle is also shown. The significant change in the interaction coefficient highlights the need to account for finite deformations.
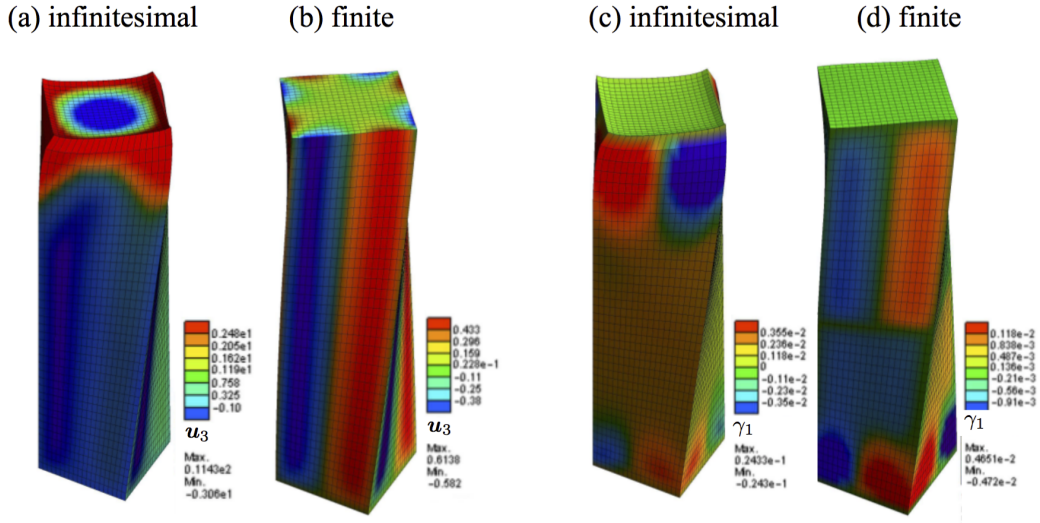

(a) infinitesimal   (b) finite   (c) infinitesimal   (d) finite

Figure 3: Comparison of the infinitesimal and finite deformation theory for the problem of torsion in a bi-crystal. The z-component of the displacement is superimposed upon the deformed domain in (a)–(b), while in (c)–(d) it is the slip.
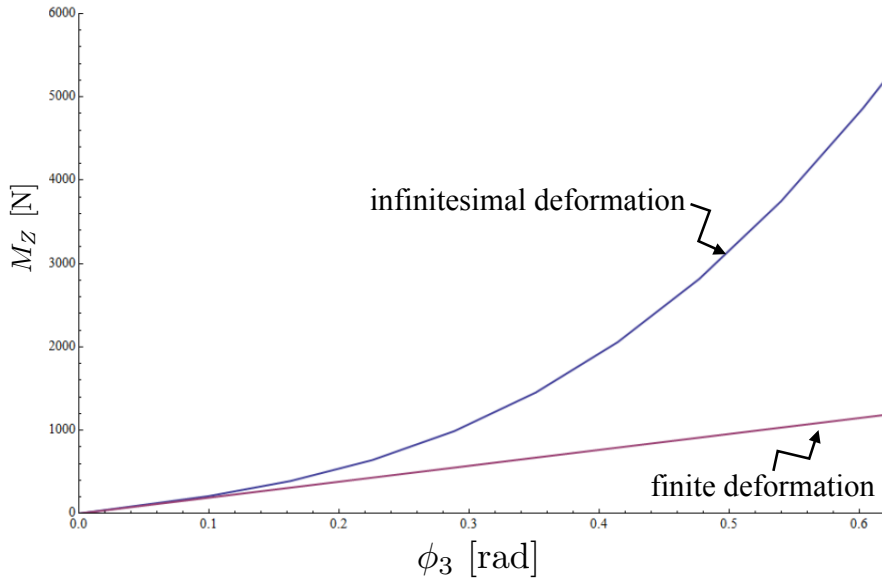

Figure 4: Relation between the applied twist ϕ_3 and the resulting torque M_z on the upper surface of the bi-crystal.

9.2 Extension of a Double-slip System Polycrystal

The focus of this example is on the misorientation of slip systems across grain boundaries. Consider the $[100]^3$ µm polycrystal subjected to tensile loading shown in Fig. 6. The polycrystal is composed of 27 equally sized grains. The direction of loading is chosen so as to ensure that the angle between the lattice orientation in each grain and the loading direction remains constant during the loading process. This ensures that the difference in the response results solely from the grain boundary model and mismatch across the grain boundary. Each of the grains has two slip systems. Consider a unit cell with $s_1 = 1/\sqrt{2}(-1, 1, 0)$ and $s_2 = 1/\sqrt{2}(1, 1, 0)$, and $m_1 = 1/\sqrt{2}(1, 1, 0)$ and $m_2 = 1/\sqrt{2}(-1, 1, 0)$. The lattice orientation of each grain in the polycrystal is defined by a rotation of the unit cell given in terms of the Euler angle $\psi=[\phi_1, \alpha, \phi_2]$, following the convention of Bunge (1969). The grains in
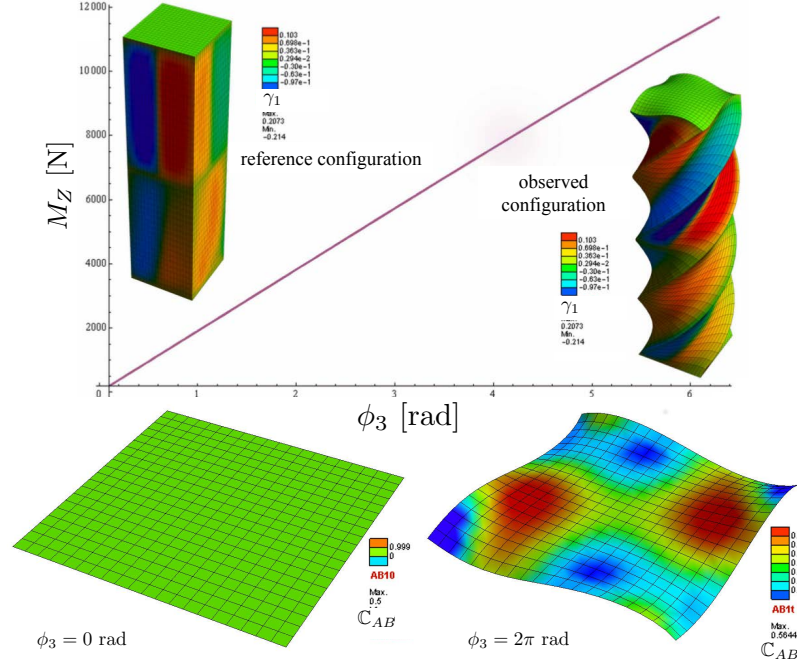
Figure 5: Relation between the applied twist ϕ_3 and the resulting torque M_z on the upper surface of the bi-crystal for the finite deformation model. The variation in the grain-boundary interaction coefficient $\overline{\mathbb{C}}_{AB}$ at various stages of the loading is also shown.

the polycrystal are either unrotated (i.e. $\psi = [0°, 0°, 0°]$) or rotated by $\psi = [-90°, \alpha°, 90°]$, where $\alpha \in [0, 90]$. This gives rise to the polycrystalline structure depicted in Fig. 7. The disctretization of the domain and the boundary conditions are shown in Fig. 6. Each grain is discretized into 6^3 elements. A displacement of $u_y = 100$ μm is applied on the boundary with outward normal $\boldsymbol{n} = [0, 1, 0]$. Micro-hard boundary conditions are also assumed on this surface. The opposite boundary with outward normal $\boldsymbol{n} = [0, -1, 0]$ is prevented from displacing in the y-direction and micro-hard conditions are imposed. The additional constraints to prevent rigid body motion are indicated in Fig. 6.
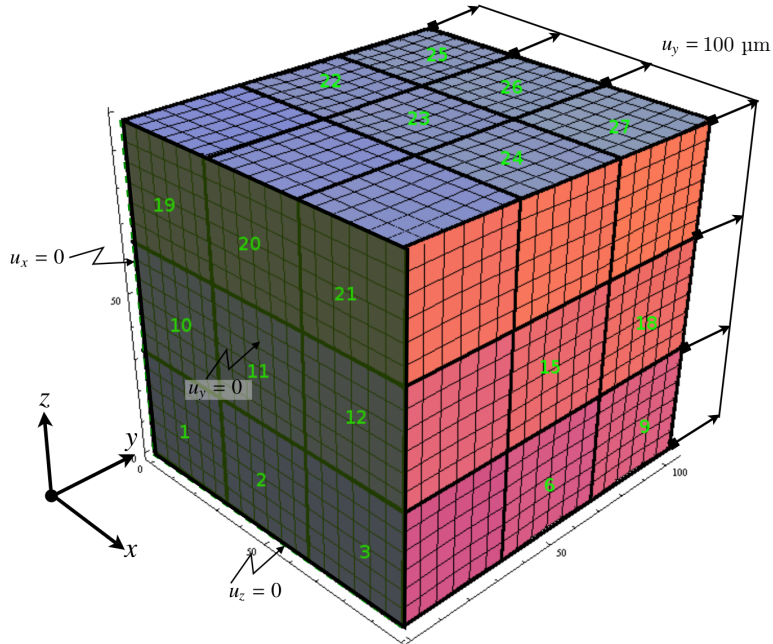

Figure 6: The problem of extension of a double-slip system polycrystal.
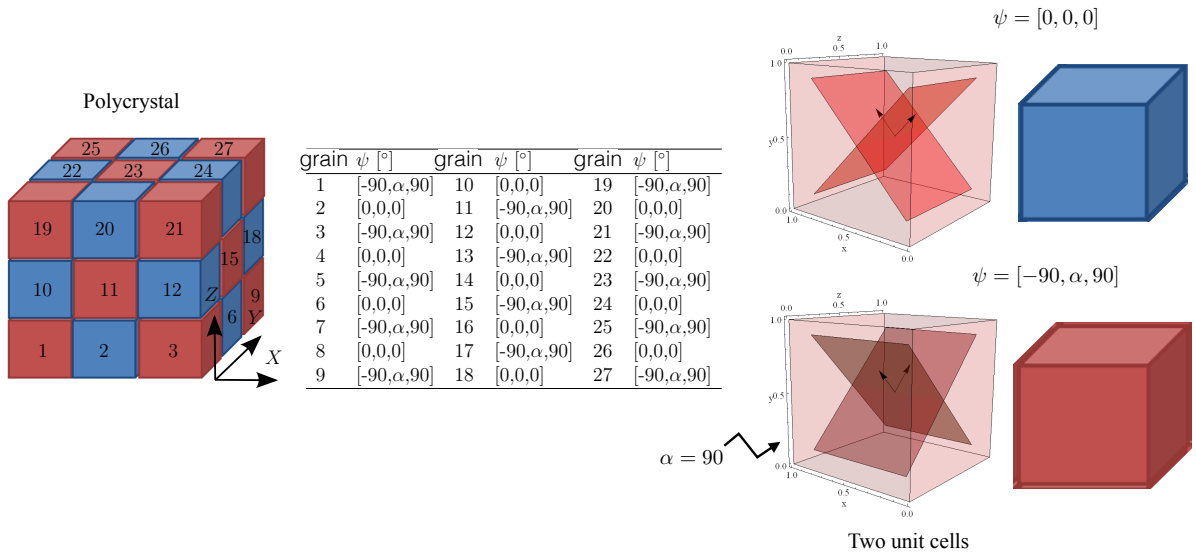
115

Polycrystal

grain	ψ [°]	grain	ψ [°]	grain	ψ [°]
1	[-90,α,90]	10	[0,0,0]	19	[-90,α,90]
2	[0,0,0]	11	[-90,α,90]	20	[0,0,0]
3	[-90,α,90]	12	[0,0,0]	21	[-90,α,90]
4	[0,0,0]	13	[-90,α,90]	22	[0,0,0]
5	[-90,α,90]	14	[0,0,0]	23	[-90,α,90]
6	[0,0,0]	15	[-90,α,90]	24	[0,0,0]
7	[-90,α,90]	16	[0,0,0]	25	[-90,α,90]
8	[0,0,0]	17	[-90,α,90]	26	[0,0,0]
9	[-90,α,90]	18	[0,0,0]	27	[-90,α,90]

$\psi = [0, 0, 0]$

$\psi = [-90, \alpha, 90]$

$\alpha = 90$

Two unit cells

Figure 7: The construction of the polycrystalline domain from two possible unit cells. The variable angle α governs the interaction between grains.

The variation in the reaction force in the e_2 direction versus the E_{22} component of the Green–Lagrange strain for differing values of α and for each of the three flow relations is shown in Fig. 8.

The Gurtin I model is able to capture the range of responses between micro-free and micro-hard as α varies between 0 and 90° as shown in Fig. 8(a). For the case of $\alpha = 0°$, the orientation of the crystal lattice is the same for all grains and, given the orientation of the grains boundaries, there is no interaction between grains. The response of the system is thus identical to that obtained using a micro-free gain boundary condition. As α is increased so the interaction between grains across the grain boundaries increases. For the case of $\alpha = 90°$, the global response of the system is identical to that obtained by assuming a micro-hard grain boundary. The micro-hard condition is often assumed in the literature in the absence of a grain boundary model such as the ones investigated here. The Gurtin I model can thus account for the full range of interaction between micro-free and micro-hard in a physical meaningful manner. The modified formulation behaves in a near-identical manner to the Gurtin I formulation as shown in Fig. 8(c).

The Gurtin II formulation is unable to account for the role of the grain boundary and behaves like the micro-free model for all values of α as shown in Fig. 8(b). This is not necessarily surprising as the Gurtin II formulation does not directly account for the misorientation of the crystal lattice in adjacent grains via a defect measure.

9.3 Nanoindentation

The current example attempts to replicate key features of the nanoindentation experiment in a FCC bi-crystal performed by Britton et al. (2009). Indentation was performed using a Berkovich indenter adjacent to a grain boundary. The simulated experiment is shown in Fig. 9. The orientation of slip systems in the (unrotated) crystal lattice are also indicated. The discretization is chosen finer in the vicinity of the grain boundary and below the contact area of the indenter. Contact is modelled by prescribing the vertical displacement of nodes below the contact point. The contact is assumed frictionless and micro-hard boundary conditions imposed below the indenter tip. The displacement on all other faces is fully constrained and micro-free conditions are assumed. The simulation was performed using the finite deformation theory. Two different grain boundary misorientations were examined: a low-angle grain boundary with a misorientation of 10° and a high-angle grain boundary with a misorientation of 44°.

The net reaction force on the indenter versus the indentation depth for the three different plastic flow relations are shown in Fig. 10. Also shown are the results for the micro-free and micro-hard grain boundary assumptions. The Gurtin I model shows a nearly micro-free behaviour for both the high and low grain boundary misorientations with only a tiny spread between the low and high angle grain boundary. The dislocations are recombining on both sides of the boundary leading to a very small dissipation at the boundary. In the Gurtin II model the response is
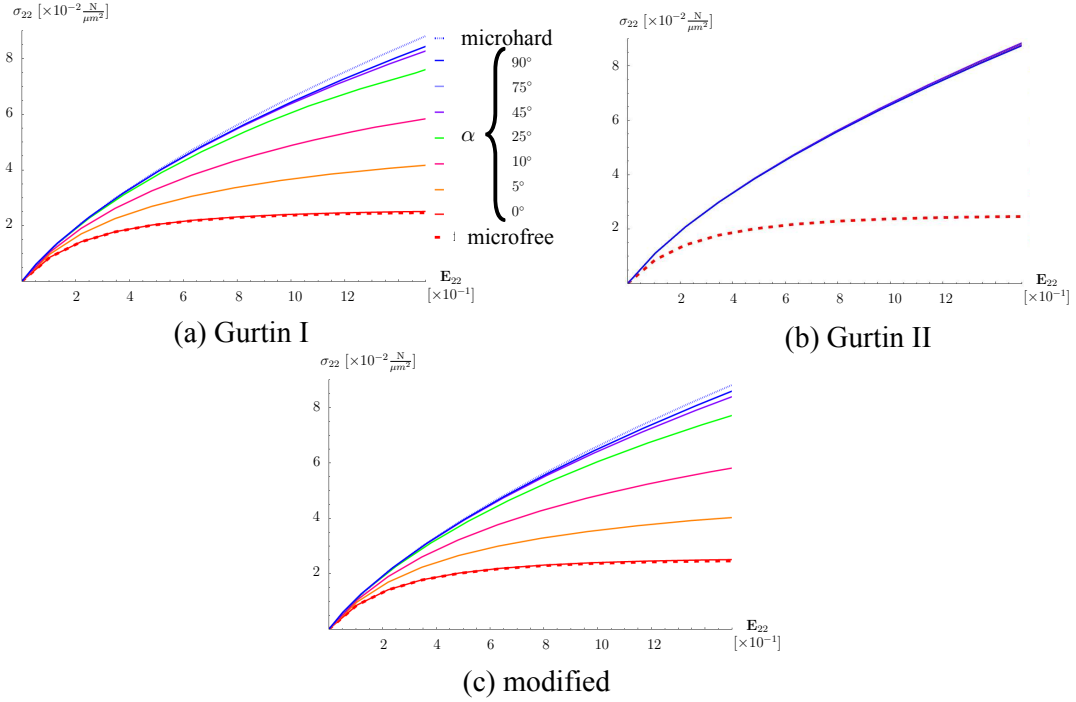
(a) Gurtin I

(b) Gurtin II

(c) modified

Figure 8: The relation between the reaction force and the strain on the upper surface of the polycrystalline domain for varying α and for each of the three plastic flow relations.

similar to the micro-hard model with a small difference between the low- and high-angle boundary. The difference can be explained with the different crystal orientation in the second grain because of the different misorientation angle. Only the modified model produces the expected significant difference between the low- and high-angle grain boundary. The modified model is in agreement with the trends exhibited by the results in Britton et al. (2009) that show a stiffer response for the high angle grain boundary. This example also illustrates that in addition to the misorientation of adjacent grains, the orientation of the grains themselves plays a significant role in the overall response.
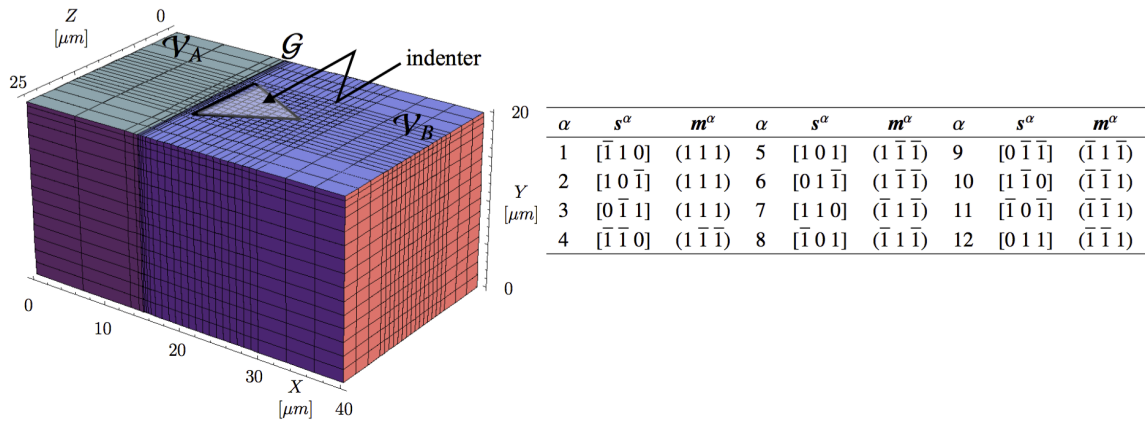

α	s^{α}	m^{α}	α	s^{α}	m^{α}	α	s^{α}	m^{α}
1	$[\bar{1}\,1\,0]$	$(1\,1\,1)$	5	$[1\,0\,1]$	$(1\,\bar{1}\,\bar{1})$	9	$[0\,\bar{1}\,\bar{1}]$	$(\bar{1}\,1\,\bar{1})$
2	$[1\,0\,\bar{1}]$	$(1\,1\,1)$	6	$[0\,1\,\bar{1}]$	$(1\,\bar{1}\,\bar{1})$	10	$[1\,\bar{1}\,0]$	$(\bar{1}\,1\,\bar{1})$
3	$[0\,\bar{1}\,1]$	$(1\,1\,1)$	7	$[1\,1\,0]$	$(\bar{1}\,1\,\bar{1})$	11	$[\bar{1}\,0\,\bar{1}]$	$(\bar{1}\,\bar{1}\,1)$
4	$[\bar{1}\,\bar{1}\,0]$	$(1\,\bar{1}\,\bar{1})$	8	$[\bar{1}\,0\,1]$	$(\bar{1}\,1\,\bar{1})$	12	$[0\,1\,1]$	$(\bar{1}\,\bar{1}\,1)$

Figure 9: The nanoindetation problem.

10   Discussion and Conclusions

The response of a polycrystalline material at small length scales and finite deformations can be modelled using the extension of the Gurtin (2008b) model presented here. Three thermodynamically consistent flow relations were proposed. The resulting finite element formulation of the highly nonlinear coupled system of governing equations is robust. The use of automatic differentiation to compute the tangent ensured quadratic convergence
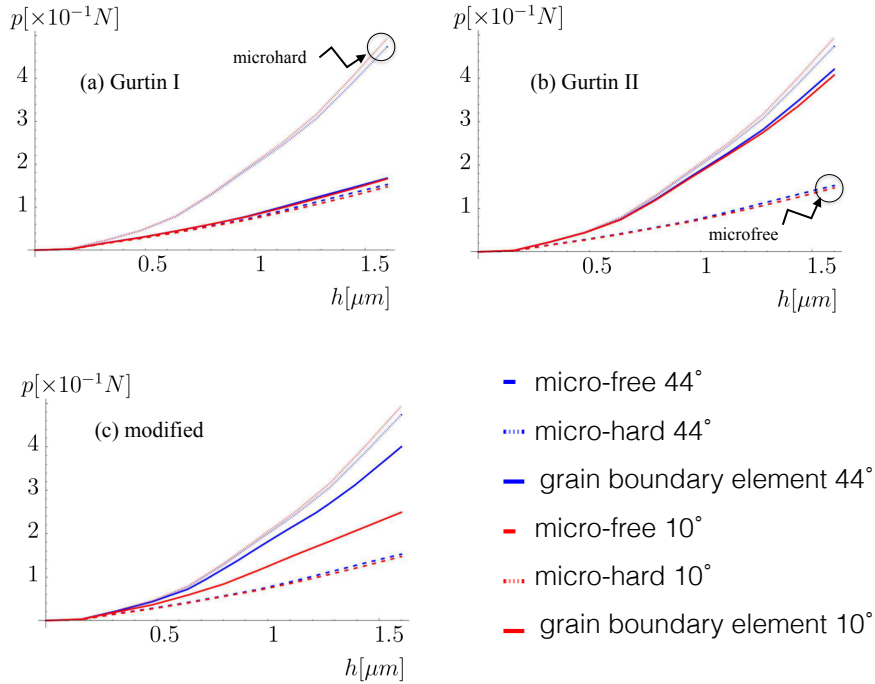
Figure 10: The relationship between the reaction force on the indenter p and the indentation depth h for the various plastic flow relations, and the low and high-angle grain boundary configuration.

of the Newton scheme. The numerical examples presented illustrate features of the flow relations and the related defect measures at the grain boundary. The examples do not necessarily identify any one model as physically correct. The nanoindentation example appears to show that only the modified formulation is capable of capturing the experimentally observed difference between the low- and high-angle grain boundary configuration.

A detailed comparison with dislocation dynamics simulations, and the careful measurement of the constitutive parameters used to calibrate the numerical examples would provide further insight.

References

Asaro, R.; Rice, J.: Strain localization in ductile single crystals. *Journal of the Mechanics and Physics of Solids*, 25, 5, (1977), 309 – 338.

Britton, T.; Randman, D.; Wilkinson, A.: Nanoindentation study of slip transfer phenomenon at grain boundaries. *Journal of Materials Research*, 24, (2009), 607–615.

Bunge, H.-J.: *Textures in Research and Practice*, chap. Textures in Three-Dimensional Pole Figures, pages 24–35. Springer-Verlag, Berlin (1969).

Cermelli, P.; Gurtin, M.: On the characterization of geometrically necessary dislocations in finite plasticity. *Journal of the Mechanics and Physics of Solids*, 49, 7, (2001), 1539 – 1568.

Evers, L.; Brekelmans, W.; Geers, M.: Scale dependent crystal plasticity framework with dislocation density and grain boundary effects. *International Journal of Solids and Structures*, 41, (2004), 5209 – 5230.

Gottschalk, D.; McBride, A.; Reddy, B. D.; Javili, A.; Wriggers, P.; Hirschberger, C. B.: Computational and theoretical aspects of a grain-boundary model that accounts for grain misorientation and grain-boundary orientation. *ArXiv e-prints*.

Gottschalk, D.; Mcbride, A.; Reddy, B. D.; Javili, A.; Wriggers, P.; Hirschberger, C. B.: Computational and theoretical aspects of a grain-boundary model that accounts for grain misorientation and grain-boundary orientation. *Computational Materials Science*, 111, (2015), 443–459.

Gurtin, M.: A gradient theory of single-crystal plasticity that accounts for geometrically necessary dislocations. *Journal of the Mechanics and Physics of Solids*, 50, 1, (2002), 5 – 32.

Gurtin, M.: The Burgers vector and the flow of screw and edge dislocations in finite-deformation single-crystal plasticity. *Journal of the Mechanics and Physics of Solids*, 54, 9, (2006), 1882 – 1898.

Gurtin, M.: A finite-deformation, gradient theory of single-crystal plasticity with free energy dependent on densities of geometrically necessary dislocations. *International Journal of Plasticity*, 24, 4, (2008a), 702 – 725.

Gurtin, M.: A theory of grain boundaries that accounts automatically for grain misorientation and grain-boundary orientation. *Journal of the Mechanics and Physics of Solids*, 56, 2, (2008b), 640 – 662.

Gurtin, M.; Needleman, A.: Boundary conditions in small-deformation, single-crystal plasticity that account for the burgers vector. *Journal of the Mechanics and Physics of Solids*, 53, 1, (2005), 1 – 31.

Gurtin, M. E.; Murdoch, A. I.: A continuum theory of elastic material surfaces. *Archive for Rational Mechanics and Analysis*, 57, 4, (1975), 291–323.

Hill, R.; Rice, J.: Constitutive analysis of elastic-plastic crystals at arbitrary strain. *Journal of the Mechanics and Physics of Solids*, 20, 6, (1972), 401–413.

Holzapfel, G. A.: *Nonlinear solid mechanics: a continuum approach for engineering*. John Wiley & Sons Ltd. (2000).

Javili, A.; McBride, A.; Steinmann, P.; Reddy, B.: A unified computational framework for bulk and surface elasticity theory: a curvilinear-coordinate-based finite element methodology. *Computational Mechanics*, 54, 3, (2014), 745–762.

Korelc, J.: Multi-language and multi-environment generation of nonlinear finite element codes. *Engineering with Computers*, 18, 4, (2002), 312–327.

Lee, E. H.: Elastic–plastic deformation at finite strain. *Journal of Applied Mechanics*, 36, (1969), 1–6.

Rice, J. R.: Inelastic constitutive relations for solids: An internal-variable theory and its application to metal plasticity. *Journal of the Mechanics and Physics of Solids*, 19, 6, (1971), 433–455.

Steinmann, P.; Stein, E.: On the numerical treatment and analysis of finite deformation ductile single crystal plasticity. *Computer Methods in Applied Mechanics and Engineering*, 129, 3, (1996), 235–254.

van Beers, P.; McShane, G.; Kouznetsova, V.; Geers, M.: Grain boundary interface mechanics in strain gradient crystal plasticity. *Journal of the Mechanics and Physics of Solids*, 61, 12, (2013), 2659 – 2679.

Address: Centre for Research in Computational and Applied Mechanics, University of Cape Town, 5th floor, Menzies Building, Private Bag X3, 7701 Rondebosch, South Africa Tel: + 27 21 650-3817 Fax: + 27 21 685-2281
email: `{andrew.mcbride, daya.reddy}@uct.ac.za`

Address: Institute of Continuum Mechanics, Leibniz Universität Hannover, Appelstrasse 11, 30167 Hannover, Germany
email: `daniel_gottschalk@web.de` and `wriggers@ikm.uni-hannover.de`

Address: Department of Civil and Environmental Engineering, Stanford University, Stanford, CA 94305, USA
email: `ajavili@stanford.edu`